Electrochemical behavior of Sn–Fe alloy film negative electrodes for a sodium secondary battery using inorganic ionic liquid Na[FSA]–K[FSA]

Takayuki Yamamoto[a], Toshiyuki Nohira[b,*], Rika Hagiwara[a,*], Atsushi Fukunaga[c], Shoichiro Sakai[c], Koji Nitta[c]

[a] Graduate School of Energy Science, Kyoto University, Yoshida-honmachi, Sakyo-ku, Kyoto 606-8501, Japan

[b] Institute of Advanced Energy, Kyoto University, Gokasho, Uji, 611-0011, Japan

[c] Sumitomo Electric Industries Ltd., 1-1-3 Shimaya, Konohana-ku, Osaka 554-0024, Japan

* Corresponding Authors:

E-mail: nohira.toshiyuki.8r@kyoto-u.ac.jp, hagiwara@energy.kyoto-u.jp,

Tel: +81-75-753-5822, Fax: +81-75-753-5906

Abstract

Sn–Fe alloy thin films were prepared by electroplating of tin on iron substrates and annealing them at 533 K for 0 to 25 h. The charge–discharge behavior of the films as negative electrodes for sodium secondary batteries was evaluated using a Na[FSA]–K[FSA] (FSA = bis(fluorosulfonyl)amide) ionic liquid at 363 K. Although the Sn–Fe film without annealing (pure Sn film) showed a relatively high discharge capacity of 730 mAh $(g\text{-}Sn)^{-1}$ in the first cycle, its capacity rapidly decreased to 30 mAh $(g\text{-}Sn)^{-1}$ within 10 cycles. In contrast, Sn–Fe films annealed for 2 or 4 h retained higher

discharge capacities of 191 or 82 mAh (g-Sn)$^{-1}$ after 100 cycles, respectively, due to the formation of an $FeSn_2$ alloy. Additionally, an $FeSn_2$ film was prepared by removing the SnO layer of the Sn–Fe alloy film that was annealed for 25 h, and its charge–discharge behavior was investigated.

Keywords: Sodium secondary battery, Ionic liquid, Sn–Fe alloy, Negative electrode

1. Introduction

Sodium secondary battery is a promising alternative to the widely used lithium-ion battery (LIB), due to abundant sodium resources in the Earth's crust and in sea water, and sodium being chemically similar to lithium. The number of papers on sodium secondary batteries has increased rapidly in the last decade [1–9]. However, because most of the previous studies utilized highly volatile and flammable organic solvent-based electrolytes, safety concerns from over-charging and thermal runaway remain. These concerns are especially important for large-scale battery systems in practical applications.

Based on these backgrounds, our group has focused on ionic liquid electrolytes [10–21] due to their high safety such as negligible volatility and non-flammability. Moreover, their superior physicochemical properties of reasonably high ionic conductivities and wide electrochemical windows are attractive for use in battery applications. Especially, we have intensively investigated an eutectic Na[FSA]–K[FSA] ionic liquid (x(Na[FSA]) = 0.56; FSA = bis(fluorosulfonyl)amide) [13–21]. This liquid consists of inexpensive atomic cations, and unlike bis(trifluoromethylsulfonyl)amide (TFSA)-based salts, the production of FSA salts does not require an expensive

electrolytic fluorination process. Thus, it is likely to further decrease the prices of FSA salts when their large-scale production is put into practice. Although we have reported that Na/$NaCrO_2$ and Na/$Na_2FeP_2O_7$ cells showed good cycleability and rate capability in this ionic liquid at 353–363 K [15–17], there is intrinsically a safety risk due to the use of highly reactive sodium metal negative electrode. Therefore, to develop safer negative electrode materials, we have focused on tin negative electrodes due to the high theoretical capacity of tin (847 mAh $(g\text{-}Sn)^{-1}$). We prepared tin-coated aluminum foils with 10 μm thickness of tin (hereinafter, called "Sn–Al film") by electroplating, and investigated charge–discharge behavior of the films in Na[FSA]–K[FSA] ionic liquid electrolyte at 363 K [18,19]. As a result, the Sn–Al film showed rapid capacity decline within 10 cycles from 729 to 121 mAh $(g\text{-}Sn)^{-1}$, due to large volume changes during cycling (ΔV = 424% for $Na_{15}Sn_4$) causing pulverization of the active materials.

With an aim to improve such poor cycleability, several kinds of Sn–M films (M = Cu, Ni) with a thinner tin film (~1 μm) were prepared by electroplating of tin on copper or nickel substrates and subsequent annealing of these films at 463 K [20,21]. We especially focused on the utilization of such electrodeposited films because coherent and strong interfaces between tin films and substrates could be easily prepared and they would prevent the delamination of the active material layer from the substrate, resulting in good cycleability. Moreover, since this simple electrode structure does not require conductive agents or binders, a higher capacity is expected compared to the conventional composite electrodes. Since copper and nickel do not react with sodium, it is expected that Cu–Sn and Ni–Sn alloys will also be less active and will act as buffers for the large volume changes of tin, which prevents the active materials from being electrically isolated. We evaluated the charge–discharge characteristics of the Sn–Cu

and Sn–Ni films in Na[FSA]–K[FSA] ionic liquid at 363 K. For Sn–Cu films [20], it was found that Cu_6Sn_5 slightly reacts with sodium and Cu_3Sn is practically inactive. Moreover, a Sn–Cu film annealed for 4 h (4h-annealed film) exhibited the stable reversible capacity of ca. 100–120 mAh $(g\text{-}Sn)^{-1}$ for 1000 cycles. Sn–Ni films showed different charge–discharge characteristics from the Sn–Cu films [21]. A Sn–Ni film that was not annealed (0h-annealed film) showed the highest reversible capacity of 343 mAh $(g\text{-}Sn)^{-1}$ after 100 cycles, and annealed films showed lower capacities and poorer cycleability. In addition, it turned out that Ni_3Sn_4 is almost inactive with sodium.

It is necessary to understand the electrochemical behavior of other Sn–M systems to explore new negative electrode materials for sodium secondary batteries with high charge and discharge performance. There are several reports on Sn–Fe systems for lithium-ion batteries [22–28]. It was found that the metastable $Fe_{1-x}Sn_5$ phase and the stable $FeSn_2$ phase reacted with lithium, and showed relatively high initial reversible capacities of approximately 700 and 500 mAh g^{-1}, respectively. In sodium-ion battery, it has recently been reported that $Fe_{1-x}Sn_5$ nanoparticles exhibit an initial reversible capacity of approximately 600 mAh g^{-1} [28]. However, to the best of our knowledge, there is no information on the reactivity of $FeSn_2$ with sodium.

In this study, several kinds of Sn–Fe alloy films were prepared by the electrodeposition of tin on iron substrates and subsequent annealing at 533 K, and their electrochemical behavior was investigated in Na[FSA]–K[FSA] ionic liquid at 363 K.

2. Experimental

2.1 Reagents and their handling

Na[FSA] (99+%) and K[FSA] (99+%) were purchased from Mitsubishi Materials

Electronic Chemicals Co., Ltd. The salts were dried under vacuum at 353 K for 48 h prior to use. The Na[FSA]–K[FSA] eutectic salt (x(Na[FSA]) = 0.56 [14]) was prepared by grinding the two salts in a mortar.

Tin-coated iron foils were prepared by electrodeposition of tin on iron foils. The loading mass of tin was determined to be 0.76(7) mg cm^{-2}, corresponding to 1.05(9) μm thickness of tin, by inductively coupled plasma atomic emission spectroscopy (ICP-AES). Before electrochemical measurements, these Sn–Fe films were dried under vacuum at 363 K for 48 h, and some were then annealed at 533 K under vacuum. Rotary vane pumps were used for the drying and annealing processes, and the achieved vacuum levels were approximately 1 Pa and 200 Pa, respectively. Annealing times were set for 2, 4, 10, or 25 h.

2.2 Electrochemical measurements and analysis

Galvanostatic charge–discharge tests were conducted under argon atmosphere using an electrochemical measurement apparatus (VSP, Bio-Logic Co.) with a two-electrode cell (Tomcell Japan Co., Ltd.). Two-ply glass-fiber filter papers (Whatman, GF/A, 260 μm^{t}), used as a separator, were vacuum-impregnated with the electrolyte prior to the test. The working electrode and counter electrode were Sn–Fe films and Na metal (99.85%; Sigma-Aldrich, Inc.), respectively. The charge–discharge rate was set at a current density of 84.7 mA (g-Sn)$^{-1}$, corresponding to C/10 rate. Cut-off voltages were 0.005 and 1.200 V, and the operating temperature was 363 K for all tests. The two-electrode cell was heated with a mantle heater, and its temperature was monitored by a thermocouple and maintained at 363 K.

To characterize the Sn–Fe films before and after charge–discharge tests, X-ray

diffraction (XRD) analysis was applied to identify phases of the films using an X-ray diffractometer (SmartLab, Rigaku Co.; Cu-Kα radiation (λ = 0.15418 nm)) equipped with a 1D high-speed detector (D/teX Ultra, Rigaku Co.) with a nickel filter. All XRD patterns were normalized based on the peak intensity from the Fe 211 reflection (2θ = 82.4°). The elemental compositions and chemical states of Sn–Fe alloy film were investigated by X-ray photoelectron spectroscopy (XPS; JPS-9010, JEOL) combined with argon ion etching. Surfaces and cross-sections were observed with a field emission scanning electron microscope (FE-SEM; SU-8020, Hitachi, or JSM-7600F, JEOL) with an energy dispersive X-ray spectrometer (EDX; X-max, Horiba, or X-max^{N}80, Oxford Instruments). Before the cross-sectional SEM observation, a cross-section polisher (CP; IB090-20, JEOL) was used to cut the Sn–Fe films. All charge–discharge tests were terminated at 1.200 V, and then the cells were disassembled and the Na[FSA]–K[FSA] salts on the surfaces of Sn–Fe films were removed by soaking the samples in dehydrated and deoxidized tetrahydrofuran (water content < 10 ppm, oxygen content < 1 ppm; Wako Pure Chemical Industries, Ltd.). These manipulations were conducted in the argon-filled glovebox. Finally, the samples were transferred to the analysis or work chambers of XRD, CP and FE-SEM without air exposure by using transfer vessels.

3. Results and discussion

3.1 Characterization of Sn–Fe films before charge–discharge test

3.1.1 XRD

Fig. 1 shows X-ray diffraction patterns of annealed Sn–Fe films. For the Sn–Fe film without annealing (hereinafter, called “pure Sn film”), β-Sn and Fe current collector are detected, and the diffraction peak of β-Sn 200 (2θ = 30.7°) is strong (Fig. 1a). In

addition, no peaks derived from Fe–Sn alloys ($FeSn_2$ or FeSn) are observed, indicating that Fe–Sn alloys were not formed during the drying process at 363 K for 48 h. This result is different from Sn–Cu and Sn–Ni films, in which Cu_6Sn_5 and small amounts of $NiSn_3$ were confirmed after the drying process [20,21]. After annealing at 533 K for 2 h (called "2h-annealed film", Fig. 1b), several peaks of $FeSn_2$ appear and peak intensities of β-Sn significantly decrease. This is consistent with a previous report that the rate of formation of $FeSn_2$ phase drastically increases near the melting point of tin (505 K) [29]. Moreover, a peak at 2θ = 37.2° is assigned to the SnO 002 reflection, indicating that residual oxygen is not negligible for the oxidation of β-Sn at 533 K, in a vacuum level achieved by a rotary vane pump. Peak intensities of $FeSn_2$ and SnO increase with the annealing time. In the 25h-annealed film (Fig. 1e), the peaks of pure metallic tin completely disappear, and the peaks of $FeSn_2$ and SnO are observed.

3.1.2 Cross-sectional FE-SEM

Representative cross-sectional SEM images of the annealed Sn–Fe films are shown in Fig. 2. In the pure Sn film (Fig. 2a), a β-Sn layer of 1 μm thickness is observed on the Fe current collector. In contrast, inhomogeneous growth of the $FeSn_2$ phase and the rougher Sn/Fe interface are observed in the 2h-annealed film, indicating that the formation of $FeSn_2$ proceeds from the Sn/Fe interface toward the surface of β-Sn. The $FeSn_2$ area increases in the 4h-annealed film, and the β-Sn area almost disappears in the 10h- and 25h-annealed films. Instead, a SnO layer of ca. 100 nm thickness is observed on the top surface of the 25h-annealed film (Fig. 2e).

3.2 Charge–discharge characteristics of Sn–Fe films

3.2.1 Initial charge–discharge curve

Fig. 3a and 3b show the initial charge–discharge curves for all the Sn–Fe films, and the enlarged curves for the 10h- and 25h-annealed films, respectively. Several plateaus corresponding to the alloying and dealloying of tin with sodium are observed except for the 25h-annealed film. For the pure Sn film, the initial charge (alloying) and discharge (dealloying) capacities are 836 and 730 mAh $(g\text{-}Sn)^{-1}$, respectively, that are close to the theoretical capacity of tin (847 mAh $(g\text{-}Sn)^{-1}$). During the 1st discharging process, three main plateaus are observed in the cell voltage regions of 0.10–0.11, 0.20–0.21, and 0.54–0.57 V. According to the previous studies [19, 30–32], these plateaus correspond to the coexisting states of $Na_{15}Sn_4/Na_{5-\delta}Sn_2$, $Na_{5-\delta}Sn_2$/α-NaSn, and α-NaSn/β-Sn, respectively. On the other hand, more complicated behavior is observed in the 1st charging process. Especially, several plateaus are confirmed in the region above 0.2 V, which is related to the formation of Na-poor ($x < 1$ for Na_xSn) alloy phases. However, there are few reports concerning the electrochemical formation mechanism of Na-poor phases [33]. Thus, detailed analysis will be necessary in the future. In addition, the coulombic efficiency in the 1st cycle is calculated to be 87.3%, suggesting that the irreversible reaction such as the electrolyte decomposition and the formation of solid electrolyte interphase (SEI) occur during the 1st charging process. There are several reports on SEI formation in ionic liquid electrolytes consisting of only FSA anion [34–36]. In case of silicon negative electrodes combined with LiFSA–PYR_{13}FSA ionic liquid electrolytes for lithium battery [34], the most probable species of SEI layer are LiF, sulfates, sulfites, and sulfides. Moreover, LiF is considered to be formed on the surface of lithium metal negative electrodes in FSA-based ionic liquid electrolytes [35,36]. Thus, the formation of NaF and sulfur-based compounds on the surface of tin

electrodes is speculated for the present study of sodium battery.

The initial discharge capacities are 443, 173, and 52 mAh $(g\text{-}Sn)^{-1}$ for the 2h-, 4h, and 10h-annealed films, respectively. Smaller discharge capacities are observed for Sn–Fe films with longer annealing times because the amount of active β-Sn decreases with annealing time. Although the peaks of β-Sn have completely disappeared in the X-ray diffraction pattern (Fig. 1e), the 25h-annealed film shows an initial discharge capacity of 46 mAh $(g\text{-}Sn)^{-1}$. This is explained by the fact that the 25h-annealed film possesses a larger amount of SnO. As shown in Fig. 3b, two plateaus are observed at 0.45 V and below 0.05 V for the 25h-annealed film in the 1st charging process, and they closely resemble those for SnO negative electrodes for sodium-ion battery [37]. Taking a closer look at the 1st charge curves (Fig. 3a and 3b), the pure Sn film (without SnO) and the 25h-annealed film ($FeSn_2$ and SnO) show plateaus in the region of 0.4–0.5 V, suggesting that the formation of some Na–Sn alloys and the reduction of SnO occur in this region. For other films containing both β-Sn and SnO, the observed capacities in this region are ascribed to the sum of the two reactions. Further discussion of this matter appears in subsection 3.3.1.

3.2.2 Cycleability

Cycleability of Sn–Fe films is compared in Fig. 3c and 3d. For the pure Sn film, although the high discharge capacities of over 700 mAh $(g\text{-}Sn)^{-1}$ are observed in the 1st and 2nd cycles, the capacity rapidly decreases to below 30 mAh $(g\text{-}Sn)^{-1}$ within initial 10 cycles, which is a typical capacity fade for tin negative electrodes [18]. Although the 2h-annealed film shows the capacity decline from 443 to 122 mAh $(g\text{-}Sn)^{-1}$ within initial 10 cycles, its capacity gradually recovers after 50 cycles and reaches 191 mAh

(g-Sn)$^{-1}$ at the 100th cycle. For the 4h-annealed film, its capacity decreases from 173 to 76 mAh (g-Sn)$^{-1}$ within initial 10 cycles, and maintains at around 80 mAh (g-Sn)$^{-1}$ after 100 cycles. The 10h- and 25h-annealed films exhibit stable cycle characteristics, and retain their reversible capacities of 41 and 25 mAh (g-Sn)$^{-1}$, respectively, after 100 cycles.

Especially, since the interesting cycling behavior is confirmed for the 2h-annealed Sn–Fe film, the possible mechanism is discussed as follows. Firstly, the sudden capacity drop in the initial 10 cycles can be explained by the pulverization of the active material and the loss of electrical contact between active material and current collector, as in the case of the pure Sn film. After the 10th cycle, the capacity is stabilized at around 110–120 mAh (g-Sn)$^{-1}$ until the 50th cycle, and then gradually increases to 200 mAh (g-Sn)$^{-1}$ at the 100th cycle. Such capacity recovery of the 2h-annealed Sn–Fe film was also observed for Sn–Cu and Sn–Ni films [20,21], and can be interpreted by two main factors. One possible factor is the increase of effective surface area during cycling. As shown in Fig. 5, the surface morphology of the 2h-annealed film has become rougher after 100 cycles. With increasing cycle, the electrolyte gradually penetrates into the electrode and additionally makes a direct contact with the inside region, which leads to the decrease of the practical current density for the active materials. In this way, the increased amount of the active material can contribute to the reversible capacity. Another factor is the repairing of electrical contact during cycling. Since the melting points of sodium and tin are 371 and 505 K, respectively, both atoms can diffuse fast at the intermediate operating temperature in the present study (363 K). So, with the increase in the cycle number, the electrical contact of the pulverized tin partly recovers by the interdiffusion between the “living” active material and the “dead” active material,

which brings about the capacity increase.

3.3 Analysis of Sn–Fe films after charge–discharge tests

3.3.1 XRD

Fig. 4 compares the X-ray diffraction patterns of Sn–Fe films before and after charge–discharge tests. For the pure Sn film, the *h*00 preferred orientation of β-Sn disappears, and the pattern changes to the reported powder pattern. This change indicates that β-Sn electrochemically reacts with sodium, as was the case of our previous studies [20,21]. Similar tendencies for β-Sn are observed in other Sn–Fe films after charge–discharge tests, except for the 25h-annealed film. Since the SnO peaks have disappeared after the charge–discharge tests for the annealed Sn–Fe films, SnO reacts with sodium based on the following manner [37].

$$SnO + 2\ Na \rightarrow Sn + Na_2O \quad \text{(irreversible)} \qquad (1)$$

$$Sn + 3.75\ Na \rightleftarrows Na_{3.75}Sn \quad \text{(reversible)} \qquad (2)$$

No detection of β-Sn peaks for the 25h-annealed film can be explained by the smaller amount of initial SnO and the low crystallinity of electrochemically formed β-Sn. Peak intensities of the $FeSn_2$ phase have decreased and its orientation has slightly changed, suggesting that $FeSn_2$ is active with sodium.

3.3.2 Surface FE-SEM

Surface SEM images of Sn–Fe films are shown in the Fig. 5. All films possess smooth surfaces before charge–discharge tests. However, large cracks are seen on the surface of the pure Sn film after the test. Through EDX mapping, Fe substrate is clearly observed in the cracks. This large morphological change originates from the large

expansion and contraction of β-Sn, leading to rapid degradation of the negative electrode (Fig. 3c). Although there are no large cracks in the 2h-annealed film, large pores are observed. These pores become smaller in the Sn–Fe films with longer annealing time, resulting in smoother surface morphologies. This is consistent with smaller reversible capacities having smaller volume changes.

3.3.3 Cross-sectional FE-SEM

Fig. 6 depicts cross-sectional SEM images of Sn–Fe films after charge–discharge tests. For the pure Sn film (Fig. 6a), compared to the film before test (Fig. 2a), the thickness of the active material layer has increased more than tenfold. Moreover, the formation of large pores and a rougher top surface are observed. These morphological changes are consistent with surface SEM observations (Fig. 5b) and poor cycleability (Fig. 3c). In the 2h-annealed film, relatively large particles (white color in the image) with diameters of several micrometers are distributed in the vicinity of the Sn/Fe interface. These particles are considered as $FeSn_2$ according to the EDX analysis. Moreover, it is worth noting that some $FeSn_2$ particles are refined into smaller ones, suggesting that $FeSn_2$ particles partly react with sodium. Concerning the 4h- and 10h-annealed films, similar morphological changes are confirmed. For the 25h-annealed film, some cracks appear in the $FeSn_2$ layer due to the strain from the reaction of SnO or $FeSn_2$.

3.4 Charge–discharge mechanism of $FeSn_2$ phase

3.4.1 Preparation of an $FeSn_2$ film without a SnO layer

To prepare an $FeSn_2$ film without a SnO layer, the SnO layer of the 25h-annealed

film is removed by argon ion etching attached to the XPS apparatus. Fig. 7a describes the XPS depth profiles of the 25h-annealed film. Without argon ion etching, peaks from Sn $3d_{5/2}$ and Sn $3d_{3/2}$ are observed in the oxidized state (486.5 eV for Sn $3d_{5/2}$ and 495 eV for Sn $3d_{3/2}$). No peaks from Fe $2p_{3/2}$ and Fe $2p_{1/2}$ are detected, suggesting that the surface of the film is covered with a SnO layer. After etching for 20 s, peak intensities corresponding to tin oxides decrease and new peaks appear at around 485 and 493 eV, which are assigned to the metallic state of tin. Simultaneously, peaks from Fe $2p_{3/2}$ and Fe $2p_{1/2}$ are also observed to be in the metallic state (707 eV for Fe $2p_{3/2}$ and 720 eV for Fe $2p_{1/2}$). After etching for 40 s, peak intensities of tin in the metallic state are enhanced relative to those of tin oxide. In addition, peak intensities ascribed to Fe $2p_{3/2}$ and Fe $2p_{1/2}$ increase simultaneously.

Fig. 7b shows XRD patterns before and after argon ion etching. The diffraction peak of the SnO 002 (2θ = 37.2°) has almost disappeared after etching, indicating that most of the SnO layer has been removed. In addition, the peak intensities of $FeSn_2$ phase have slightly decreased to approximately 90% of those before etching. From this point forward, we refer to the 25h-annealed film treated with 40 s etching as the "$FeSn_2$ film".

3.4.2 Charge–discharge mechanism of an $FeSn_2$ film without a SnO layer

Fig. 8a compares the initial charge–discharge curves of the 25h-annealed film and the $FeSn_2$ film. As mentioned before, for the 25h-annealed film, the plateau corresponding to the reduction of SnO into β-Sn is observed at around 0.45 V in the 1st charge process. However, the capacity of such a plateau is negligible in the initial charge curve of $FeSn_2$ film, which is consistent with the absence of SnO confirmed by XRD (Fig. 7b). Moreover, a long plateau of approximately 300 mAh $(g\text{-}Sn)^{-1}$ is

observed below 0.05 V. According to the previous studies of Fe–Sn alloy negative electrode for lithium-ion batteries [22,23], the following mechanism has been proposed for the 1st charge (lithiation) process:

$$FeSn_2 + 8.8\ Li \rightarrow 2\ Li_{4.4}Sn + Fe \quad (3)$$

It is reasonable to consider a similar reaction for the 1st charge (sodiation) process of $FeSn_2$ phase, that is,

$$FeSn_2 + 7.5\ Na \rightarrow 2\ Na_{3.75}Sn + Fe \quad (4)$$

In the 1st discharge (desodiation) process, three distinct plateaus are observed at around 0.11, 0.22, and 0.54 V, which is the typical desodiation behavior of Na–Sn alloys [18]. Thus, the assumed whole reaction of the 1st discharge process is:

$$Na_{3.75}Sn \rightarrow Sn + 3.75\ Na \quad (5)$$

As shown in Fig. 8b, after the 2nd cycle, several plateaus are observed below 0.6 V in both the charge and discharge curves, which closely resembles the alloying and dealloying reaction of tin with sodium [18,20].

$$Sn + 3.75\ Na \rightleftarrows Na_{3.75}Sn \quad (6)$$

Fig. 9a compares the XRD patterns of $FeSn_2$ film before and after the charge–discharge test. After the test, the diffraction peak intensities of $FeSn_2$ 002 and 211 (2θ = 33.7° and 35.1°) have decreased to below 25% of initial intensities, suggesting that the large amounts of $FeSn_2$ phase have reacted with sodium. Moreover, as shown in the enlarged view of the XRD patterns (Fig. 9b), the diffraction peaks of β-Sn 200 and 101 (2θ = 30.6° and 32.0°) are newly confirmed, indicating that this β-Sn phase is formed by the electrochemical reaction of $FeSn_2$ (Equations 4–6).

Fig. 10 shows the cross-sectional SEM images of the $FeSn_2$ film before and after the charge–discharge test. The thickness of the active material layer has increased from 1 to

5 μm during the test, which is indicative of a reaction between $FeSn_2$ and Na. White particles dispersed in the active material layer are considered to be $FeSn_2$ that remain unreacted.

3.4.3 Explanation of the lower capacities for Sn–Fe films with a SnO layer

Cycle characteristics of the 25h-annealed film and $FeSn_2$ film are compared in Fig. 8c. Initial discharge capacities are 46 and 268 mAh $(g\text{-}Sn)^{-1}$ for the 25h-annealed film and $FeSn_2$ film, respectively. This difference is explained as follows. Since the 25h-annealed film possesses a relatively thick SnO layer (approximately 100 nm thickness, see Fig. 2e), the inactive byproducts such as Na_2O are produced on the electrode surface during the reduction of SnO into Sn at 0.45 V in the 1st charge process (Equation 1). In fact, as described in Fig. 11, the $FeSn_2$ layer of the 25h-annealed film is covered with a thick Na_2O layer after the charge–discharge test. Thus, sodium diffusion into the inner part of the electrode is blocked by the Na_2O layer, and most of the $FeSn_2$ layer remains unreacted and does not contribute to the charge–discharge capacity. In contrast, since the $FeSn_2$ film possesses a very small amount of SnO, little Sn and Na_2O are produced at 0.45 V and sodium can directly diffuse into the $FeSn_2$ layer. As a result, a larger amount of $FeSn_2$ reacts with sodium in the 1st charge process below 0.05 V, which leads to the larger initial discharge capacity. After the 2nd cycle, although the 25h-annealed film shows small discharge capacities below 50 mAh $(g\text{-}Sn)^{-1}$, the $FeSn_2$ film retains its capacity of over 100 mAh $(g\text{-}Sn)^{-1}$ for 25 cycles.

4. Conclusions

In this study, with the aim of exploring new negative electrode materials having high

charge–discharge performance, various kinds of Sn–Fe alloy films were prepared by annealing tin-coated iron foils at 533 K for 0 to 25 h, and their charge–discharge behaviors as negative electrode materials for sodium secondary batteries were investigated using Na[FSA]–K[FSA] ionic liquid at 363 K.

The pure Sn film (without annealing) was composed of β-Sn and Fe substrate, and showed a precipitous capacity decline from 730 to 30 mAh $(g\text{-}Sn)^{-1}$ within initial 10 cycles, which is a typical degradation of tin negative electrodes. The severe morphological changes were confirmed by surface and cross-sectional FE-SEM analyses, which indicates that the electrodeposited tin film needs some buffers relieving the strain from the large volume change of tin.

In contrast, the growth of $FeSn_2$ phase was confirmed in other films annealed at 533 K for 2–25 h. Sn–Fe films with a longer annealing time showed smaller initial capacities due to the lower sodium activity of the $FeSn_2$ phase compared to β-Sn, and especially the 2h- and 4h-annealed films exhibited higher capacities of 191 and 82 mAh $(g\text{-}Sn)^{-1}$ after 100 cycles. However, their capacity retention ratios were lower than 50% that was not sufficient for practical applications. As a result of cross-sectional FE-SEM analysis, the Sn/Fe interface did not keep the original morphologies, suggesting that the $FeSn_2$ phase reacts with sodium.

$FeSn_2$ film was prepared by removing a SnO layer on the surface of the 25h-annealed film, and the film showed the 1st discharge capacity of 268 mAh $(g\text{-}Sn)^{-1}$. Combined with XRD and FE-SEM analyses, the $FeSn_2$ phase was observed to be active with sodium, and changed into Sn–Na alloy and Fe.

As a conclusion, we succeeded in improving the charge–discharge performance of tin film electrode by utilizing Sn–Fe films. However, further study to increase reversible

capacity is needed for practical applications.

Acknowledgments

This study was partly supported by the Advanced Low Carbon Technology Research and Development Program (ALCA) of Japan Science and Technology Agency (JST), and MEXT program "Elements Strategy Initiative to Form Core Research Center" (since 2012), MEXT; Ministry of Education Culture, Sports, Science and Technology, Japan.

References

[1] M. Nishijima, I.D. Gocheva, S. Okada, T. Doi, J. Yamaki, T. Nishida, Cathode properties of metal trifluorides in Li and Na secondary batteries, J. Power Sources 190 (2009) 558–562.

[2] N. Recham, J-N. Chotard, L. Dupont, K. Djellab, M. Armand, and J-M. Tarascon, Ionothermal Synthesis of Sodium-Based Fluorophosphate Cathode Materials, J. Electrochem. Soc. 156 (2009) A993–A999.

[3] L.S. Plashnitsa, E. Kobayashi, Y. Noguchi, S. Okada, and J. Yamaki, Performance of NASICON Symmetric Cell with Ionic Liquid Electrolyte, J. Electrochem. Soc. 157 (2010) A536–A543.

[4] S. Komaba, C. Takei, T. Nakayama, A. Ogata, N. Yabuuchi, Electrochemical intercalation activity of layered $NaCrO_2$ vs. $LiCrO_2$, Electrochem. Commun. 12 (2010) 355–358.

[5] S. Komaba, W. Murata, T. Ishikawa, N. Yabuuchi, T. Ozeki, T. Nakayama, A. Ogata, K. Gotoh, K. Fujiwara, Electrochemical Na Insertion and Solid Electrolyte

Interphase for Hard-Carbon Electrodes and Application to Na-Ion Batteries, Adv. Funct. Mater. 21(2011) 3859–3867.

[6] P. Senguttuvan, G. Rousse, V. Seznec, J.M. Tarascon, M.R. Palacín, $Na_2Ti_3O_7$: Lowest Voltage Ever Reported Oxide Insertion Electrode for Sodium Ion Batteries, Chem. Mater. 23 (2011) 4109–4111.

[7] N. Yabuuchi, M. Kajiyama, J. Iwatate, H. Nishikawa, S. Hitomi, R. Okuyama, R. Usui, Y. Yamada and S. Komaba, P2-type $Na_x[Fe_{1/2}Mn_{1/2}]O_2$ made from earth-abundant elements for rechargeable Na batteries, Nat. Mater. 11 (2012) 512–517.

[8] S. Komaba, Y. Matsuura, T. Ishikawa, N. Yabuuchi, W. Murata, S. Kuze, Redox reaction of Sn-polyacrylate electrodes in aprotic Na cell, Electrochem. Commun. 21 (2012) 65–68.

[9] P. Barpanda, G. Oyama, S. Nishimura, S-C. Chung, A. Yamada, A 3.8-V earth-abundant sodium battery electrode, Nat. Commun. 5 (2014) 4358.

[10] R. Hagiwara, K. Tamaki, K. Kubota, T. Goto, T. Nohira, Thermal Properties of Mixed Alkali Bis(trifluoromethylsulfonyl)amides, J. Chem. Eng. Data 53 (2008) 355–358.

[11] K. Kubota, K. Tamaki, T. Nohira, T. Goto, R. Hagiwara, Electrochemical properties of alkali bis(trifluoromethylsulfonyl)amides and their eutectic mixtures, Electrochim. Acta 55 (2010) 1113–1119.

[12] T. Nohira, T. Ishibashi, R. Hagiwara, Properties of an intermediate temperature ionic liquid NaTFSA–CsTFSA and charge–discharge properties of $NaCrO_2$ positive electrode at 423 K for a sodium secondary battery, J. Power Sources 205 (2012) 506–509.

[13] K. Kubota, T. Nohira, T. Goto, R. Hagiwara, Novel inorganic ionic liquids possessing low melting temperatures and wide electrochemical windows: Binary mixtures of alkali bis(fluorosulfonyl)amides, Electrochem. Commun. 10 (2008) 1886–1888.

[14] K. Kubota, T. Nohira, R. Hagiwara, Thermal Properties of Alkali Bis(fluorosulfonyl)amides and Their Binary Mixtures, J. Chem. Eng. Data 55 (2010) 3142–3146.

[15] A. Fukunaga, T. Nohira, Y. Kozawa, R. Hagiwara, S. Sakai, K. Nitta, S. Inazawa, Intermediate–temperature ionic liquid NaFSA–KFSA and its application to sodium secondary batteries, J. Power Sources 209 (2012) 52–56.

[16] C.Y. Chen, K. Matsumoto, T. Nohira, R. Hagiwara, A. Fukunaga, S. Sakai, K. Nitta, Shinji Inazawa, Electrochemical and structural investigation of $NaCrO_2$ as a positive electrode for sodium secondary battery using inorganic ionic liquid NaFSA–KFSA, J. Power Sources 237 (2013) 52–57.

[17] C.Y. Chen, K. Matsumoto, T. Nohira, R. Hagiwara, Y. Orikasa, Y. Uchimoto, Pyrophosphate $Na_2FeP_2O_7$ as a low-cost and high-performance positive electrode material for sodium secondary batteries utilizing an inorganic ionic liquid, J. Power Sources 246 (2014) 783–787.

[18] T. Yamamoto, T. Nohira, R. Hagiwara, A. Fukunaga, S. Sakai, K. Nitta, S. Inazawa, Charge–discharge behavior of tin negative electrode for a sodium secondary battery using intermediate temperature ionic liquid sodium bis(fluorosulfonyl)amide–potassium bis(fluorosulfonyl)amide, J. Power Sources 217 (2012) 479–484.

[19] T. Yamamoto, T. Nohira, R. Hagiwara, A. Fukunaga, S. Sakai, K. Nitta, S.

Inazawa, Thermodynamic studies on Sn–Na alloy in an intermediate temperature ionic liquid NaFSA–KFSA at 363 K, J. Power Sources 237 (2013) 98–103.

[20] T. Yamamoto, T. Nohira, R. Hagiwara, A. Fukunaga, S. Sakai, K. Nitta, S. Inazawa, Improved cyclability of Sn–Cu film electrode for sodium secondary battery using inorganic ionic liquid electrolyte, Electrochim. Acta 135 (2014) 60–67.

[21] T. Yamamoto, T. Nohira, R. Hagiwara, A. Fukunaga, S. Sakai, K. Nitta, Charge–discharge behavior of Sn–Ni alloy film electrodes in an intermediate temperature ionic liquid for the electrolyte of a sodium secondary battery, Electrochim. Acta 193 (2016) 275–283.

[22] O. Mao, R.A. Dunlap, and J.R. Dahn, Mechanically Alloyed Sn-Fe(-C) Powders as Anode Materials for Li-Ion Batteries I. The Sn_2Fe-C System, J. Electrochem. Soc. 146 (1999) 405–413.

[23] S..Yoon, J.M. Lee, H. Kim, D. Im, S.G. Doo, H.J. Sohn, An Sn–Fe/carbon nanocomposite as an alternative anode material for rechargeable lithium batteries, Electrochim. Acta 54 (2009) 2699–2705.

[24] X.L. Wang, W.Q. Han, J. Chen, and J. Graetz, Single-Crystal Intermetallic M–Sn (M = Fe, Cu, Co, Ni) Nanospheres as Negative Electrodes for Lithium-Ion Batteries, ACS Appl. Mater. Interfaces 2 (2010) 1548–1551.

[25] M. Chamas, P.E. Lippens, J.C. Jumas, K. Boukerma, R. Dedryvère, Danielle Gonbeau, J. Hassoun, S. Panero, B. Scrosati, Comparison between microparticles and nanostructured particles of $FeSn_2$ as anode materials for Li-ion batteries, J. Power Sources 196 (2011) 7011–7015.

[26] X.L. Wang, M. Feygenson, H. Chen, C.H. Lin, W. Ku, J. Bai, M.C. Aronson, T.A.

Tyson, and W.Q. Han, Nanospheres of a New Intermetallic $FeSn_5$ Phase: Synthesis, Magnetic Properties and Anode Performance in Li-ion Batteries, J. Am. Chem. Soc. 133 (2011) 11213–11219.

[27] U.G. Nwokeke, F. Nacimiento, R.Alcántara, and J.L. Tirado, $FeSn_2$-Polyacrylonitrile Electrode Obtained by Using High-Intensity Ultrasonication, Electrochem. Solid-State Lett. 14 (2011) A148–A150.

[28] F.X. Xin, H.J. Tian, X.L. Wang, W. Xu, W.G. Zheng, and W.Q. Han, Enhanced Electrochemical Performance of $Fe_{0.74}Sn_5$@Reduced Graphene Oxide Nanocomposite Anodes for Both Li-Ion and Na-Ion Batteries, ACS Appl. Mater. Interfaces 7 (2015) 7912–7919.

[29] T.J. Crichton and J.P.G. Farr, The Effect of Heat Treatment on the Fe–Sn Alloy System, Trans. Inst. Met. Fin. 82 (2004) 169–173.

[30] L. Baggetto, P. Ganesh, R.P. Meisner, R.R. Unocic, J.C. Jumas, C.A. Bridges, G.M. Veith, Characterization of sodium ion electrochemical reaction with tin anodes: Experiment and theory, J. Power Sources 234 (2013) 48–59.

[31] Z. Du, R.A. Dunlap, M.N. Obrovac, Investigation of the reversible sodiation of Sn foil by ex-situ X-ray diffractometry and Mössbauer effect spectroscopy, J. Alloys Compd. 617 (2014) 271–276.

[32] L. Baggetto, C.A. Bridges, J.C. Jumas, D.R. Mullins, K.J. Carroll, R.A. Meisner, E.J. Crumlin, X. Liu, W. Yang, and G.M. Veith, The local atomic structure and chemical bonding in sodium tin phases, J. Mater. Chem. A 2 (2014) 18959–18973.

[33] L.D. Ellis, T.D. Hatchard, and M.N. Obrovac, Reversible Insertion of Sodium in Tin, J. Electrochem. Soc. 159 (2012) A1801–A1805.

[34] D.M. Piper, T. Evans, K. Leung, T. Watkins, J. Olson, S.C. Kim, S.S. Han, V. Bhat,

K.H. Oh, D.A. Buttry, S.H. Lee, Stable silicon-ionic liquid interface for next-generation lithium-ion batteries, Nat. Commun. 6 (2015) 6230.

[35] A. Budi, A. Basile, G. Opletal, A.F. Hollenkamp, A.S. Best, R.J. Rees, A.I. Bhatt, A.P. O'Mullane, and S.P. Russo, Study of the Initial Stage of Solid Electrolyte Interphase Formation upon Chemical Reaction of Lithium Metal and N-Methyl-N-Propyl-Pyrrolidinium-Bis(Fluorosulfonyl)Imide, J. Phys. Chem. C 116 (2012) 19789−19797.

[36] A.I. Bhatt, P. Kao, A.S. Best, and A.F. Hollenkamp, Understanding the Morphological Changes of Lithium Surfaces during Cycling in Electrolyte Solutions of Lithium Salts in an Ionic Liquid, J. Electrochem. Soc. 160 (2013) A1171–A1180.

[37] M. Shimizu, H. Usui, H. Sakaguchi, Electrochemical Na-insertion/extraction properties of SnO thick-film electrodes prepared by gas-deposition, J. Power Sources 248 (2014) 378–382.

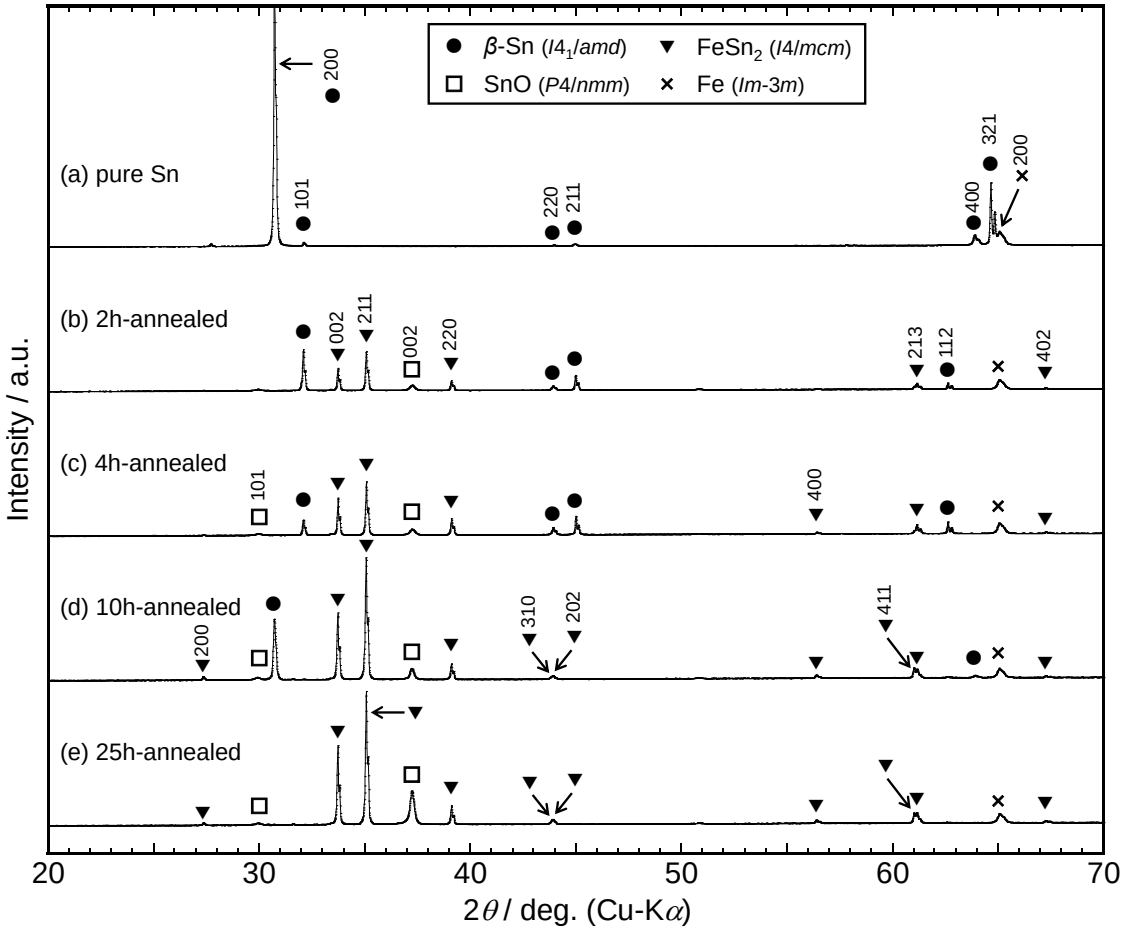

Fig. 1. XRD patterns of annealed Sn–Fe films. Annealing temperature: 533 K. Annealing time: 0–25 h.

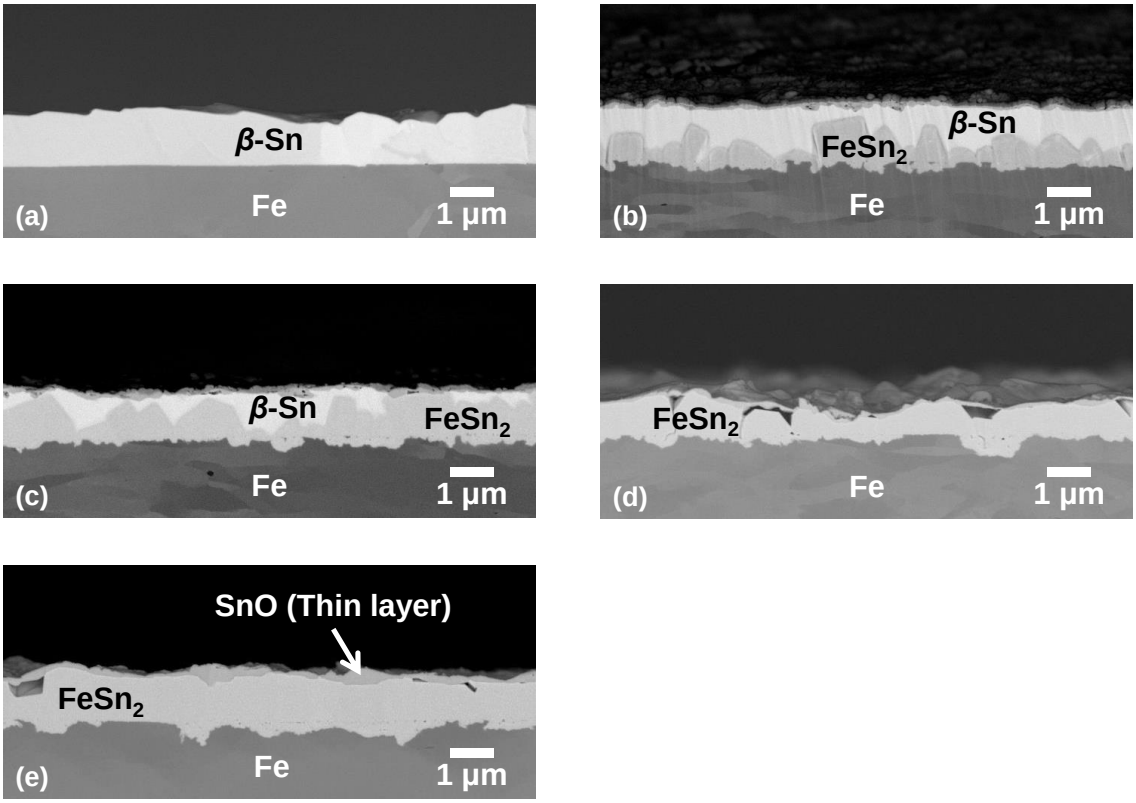

Fig. 2. Selected cross-sectional FE-SEM images of annealed Sn–Fe films. (a) pure Sn, (b) 2h-annealed, (c) 4h-annealed, (d) 10h-annealed, and (e) 25h-annealed.

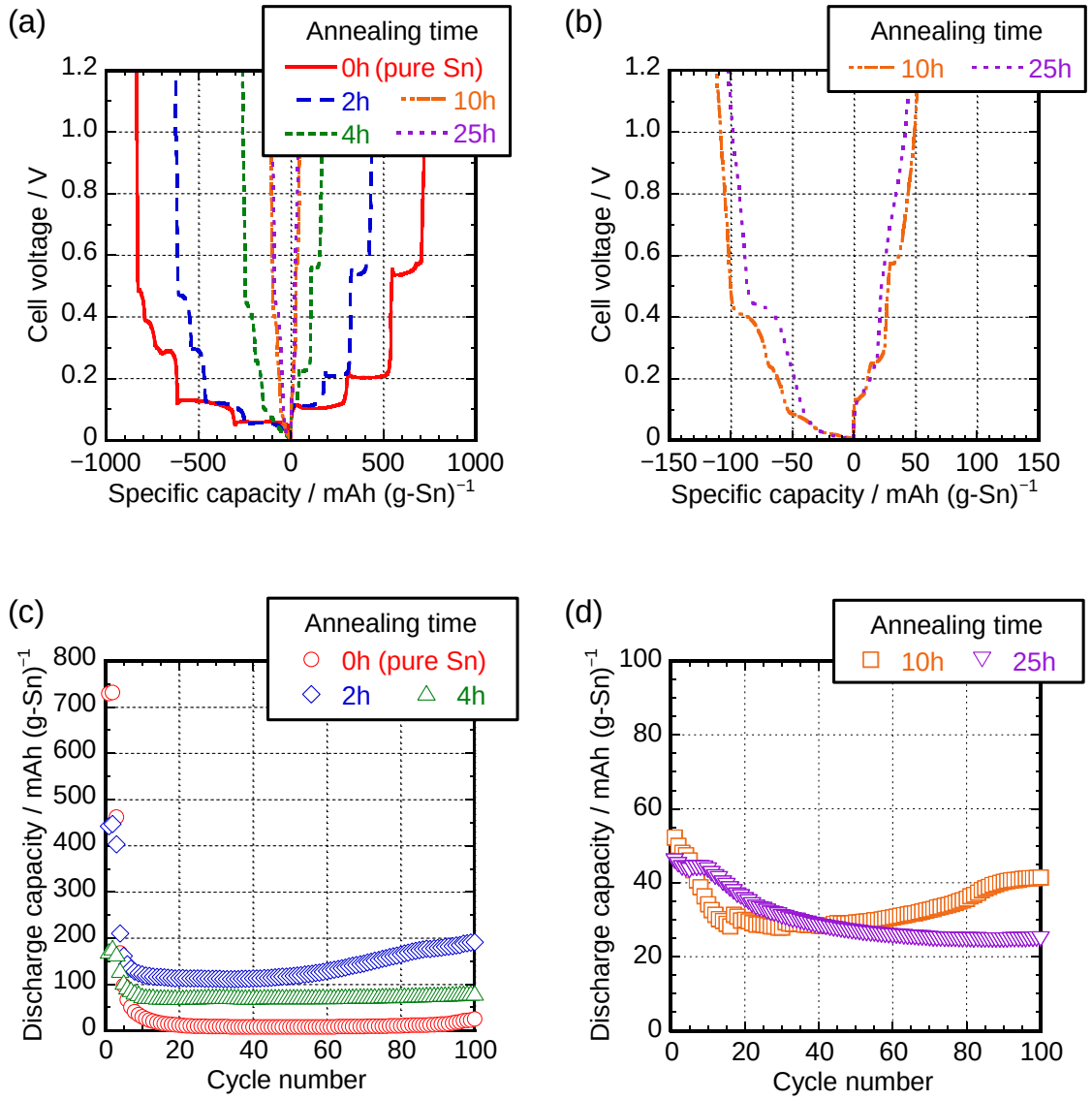

Fig. 3. (a) and (b) Initial charge–discharge curves of Sn–Fe films at a current density of 84.7 mA (g-Sn)$^{-1}$. (c) and (d) Cycle characteristics of these Sn–Fe films for 100 cycles.

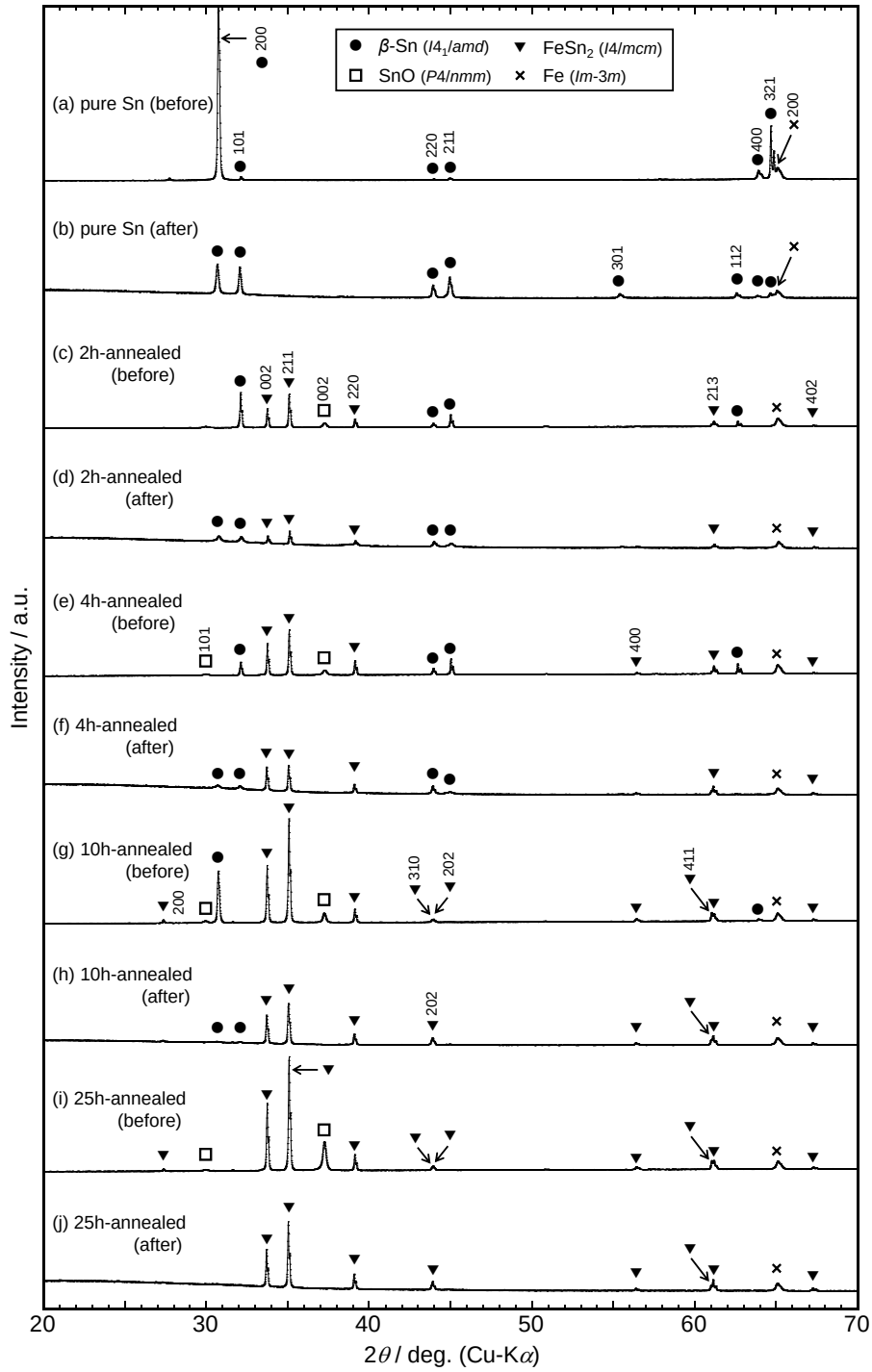

Fig. 4. Comparison of the XRD patterns of Sn–Fe films before and after 100 cycles of charge–discharge. (a) pure Sn, before, (b) pure Sn, after, (c) 2h-annealed, before, (d) 2h-annealed, after, (e) 4h-annealed, before, (f) 4h-annealed, after, (g) 10h-annealed, before, (h) 10h-annealed, after, (i) 25h-annealed, before, (j) 25h-annealed, after.

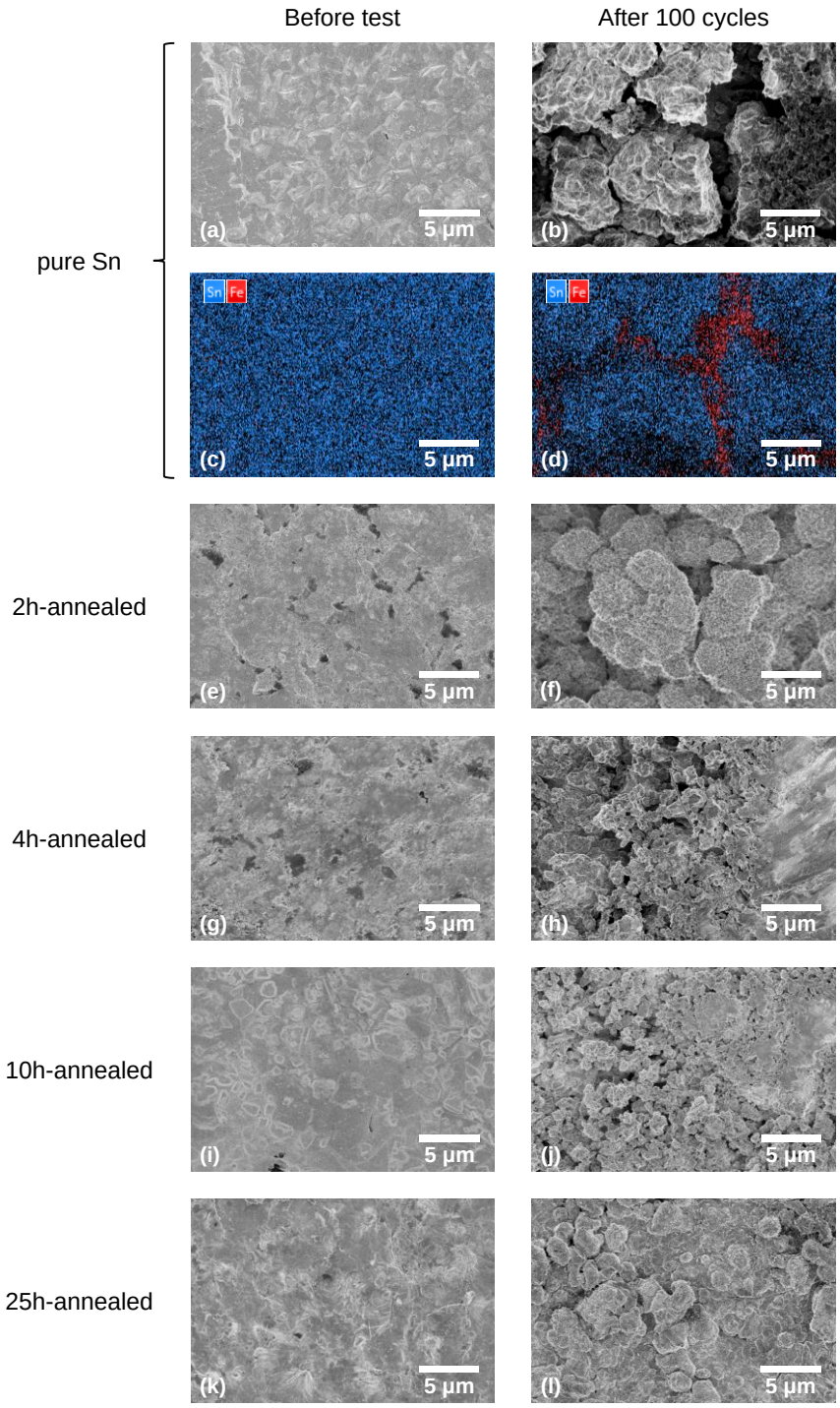

Fig. 5. Representative surface SEM and EDX mapping images of Sn–Fe films before and after 100 cycles of charge–discharge. (a) and (c) pure Sn, before, (b) and (d) pure Sn, after, (e) 2h-annealed, before, (f) 2h-annealed, after, (g) 4h-annealed, before, (h) 4h-annealed, after, (i) 10h-annealed, before, (j) 10h-annealed, after, (k) 25h-annealed, before, (l) 25h-annealed, after.

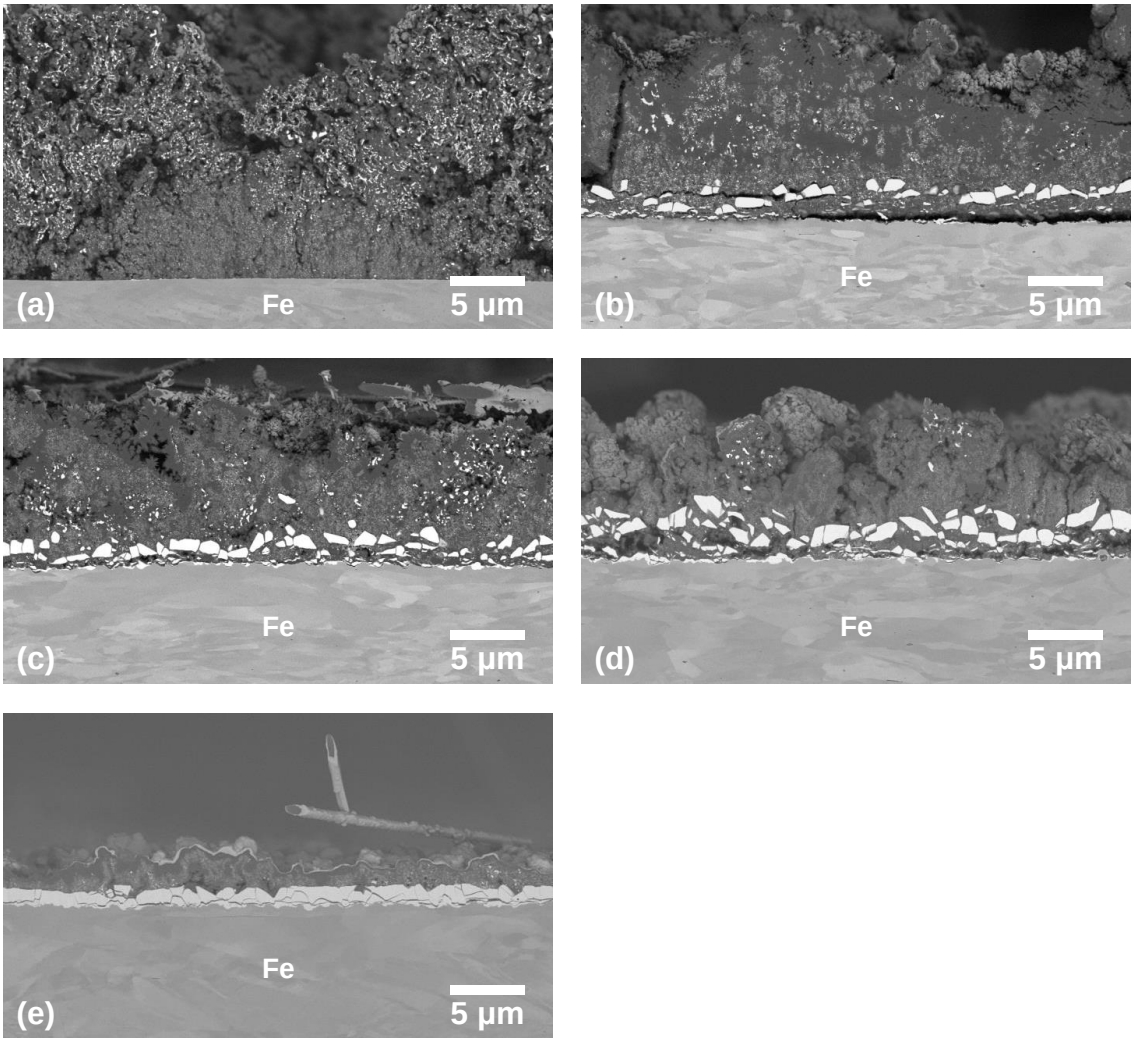

Fig. 6. Selected cross-sectional SEM images of Sn–Fe films after 100 cycles of charge–discharge. (a) pure Sn, (b) 2h-annealed, (c) 4h-annealed, (d) 10h-annealed, (e) 25h-annealed.

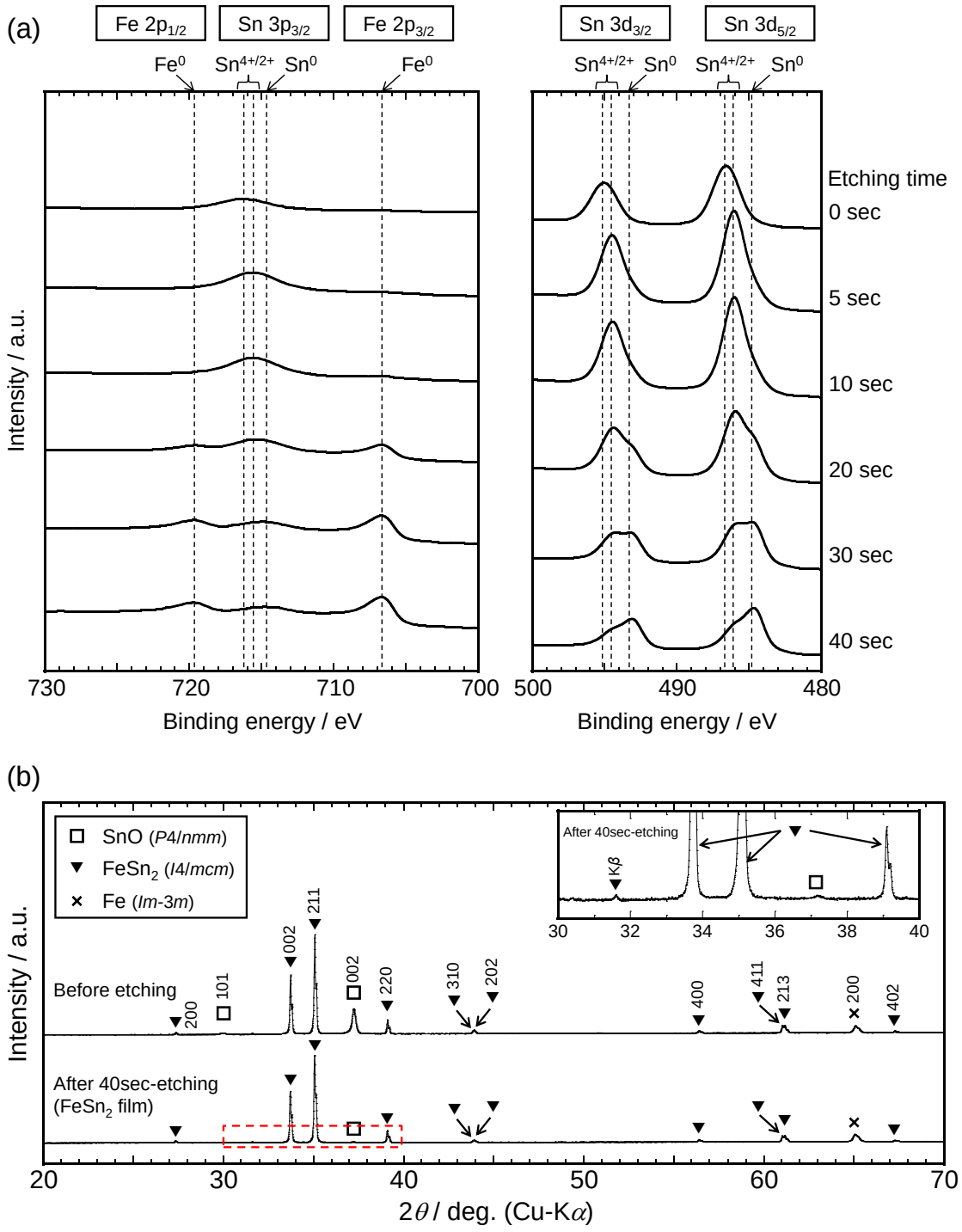

Fig. 7. (a) XPS depth profiles of 25h-annealed Sn–Fe films and (b) comparison of the XRD patterns of 25h-annealed Sn–Fe film electrodes before and after 40sec-etching. Inset shows the enlarged views of the red rectangular region.

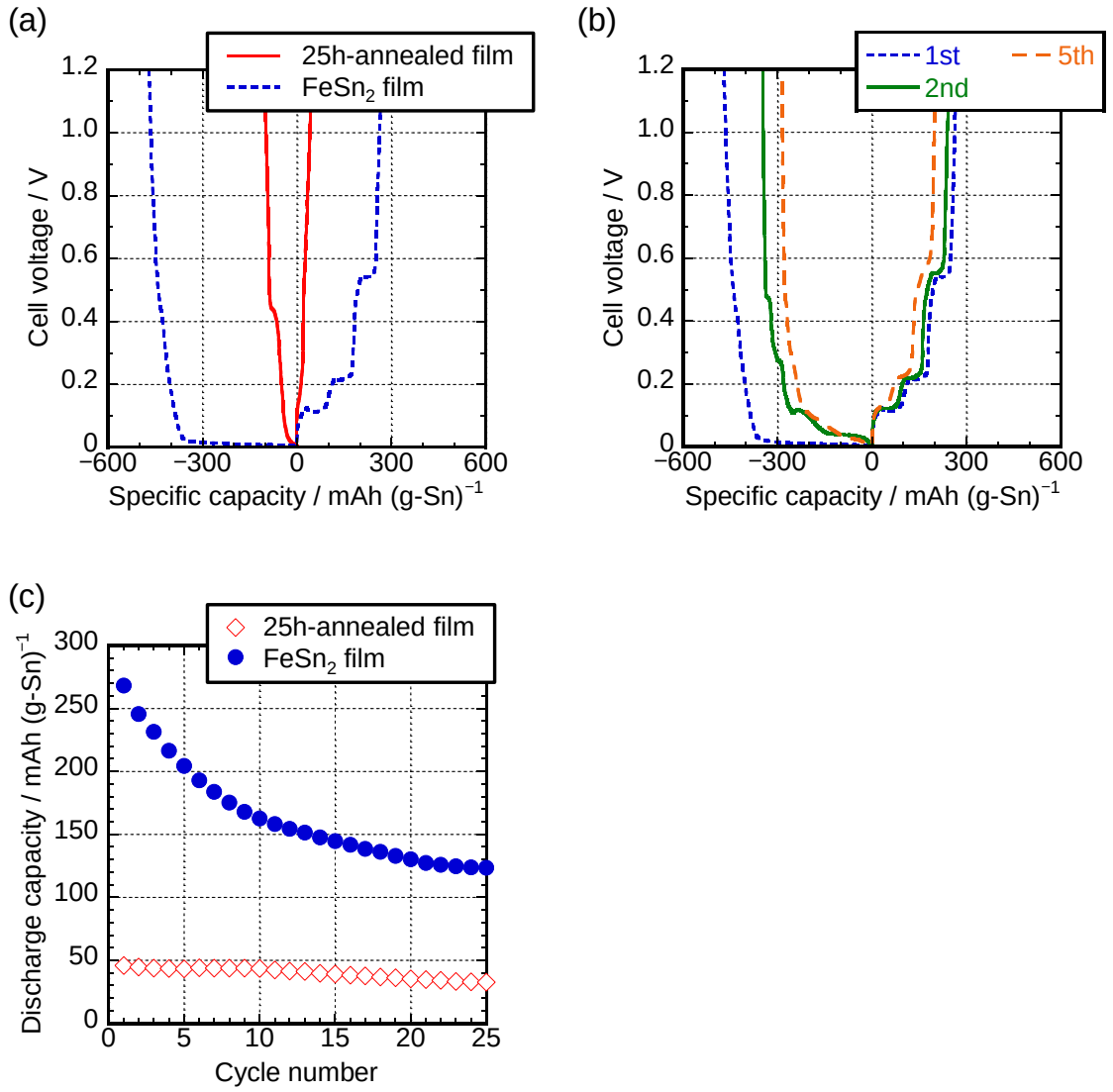

Fig. 8. (a) Initial charge–discharge curves of the 25h-annealed film and $FeSn_2$ film. Current density: 84.7 mA $(g\text{-}Sn)^{-1}$. Cut-off voltages: 0.005–1.200 V. (b) Charge–discharge curves of the 25h-annealed film and $FeSn_2$ film. Cycle number: 1st, 2nd, and 5th. (c) Cycle characteristics of these Sn–Fe films for 25 cycles.

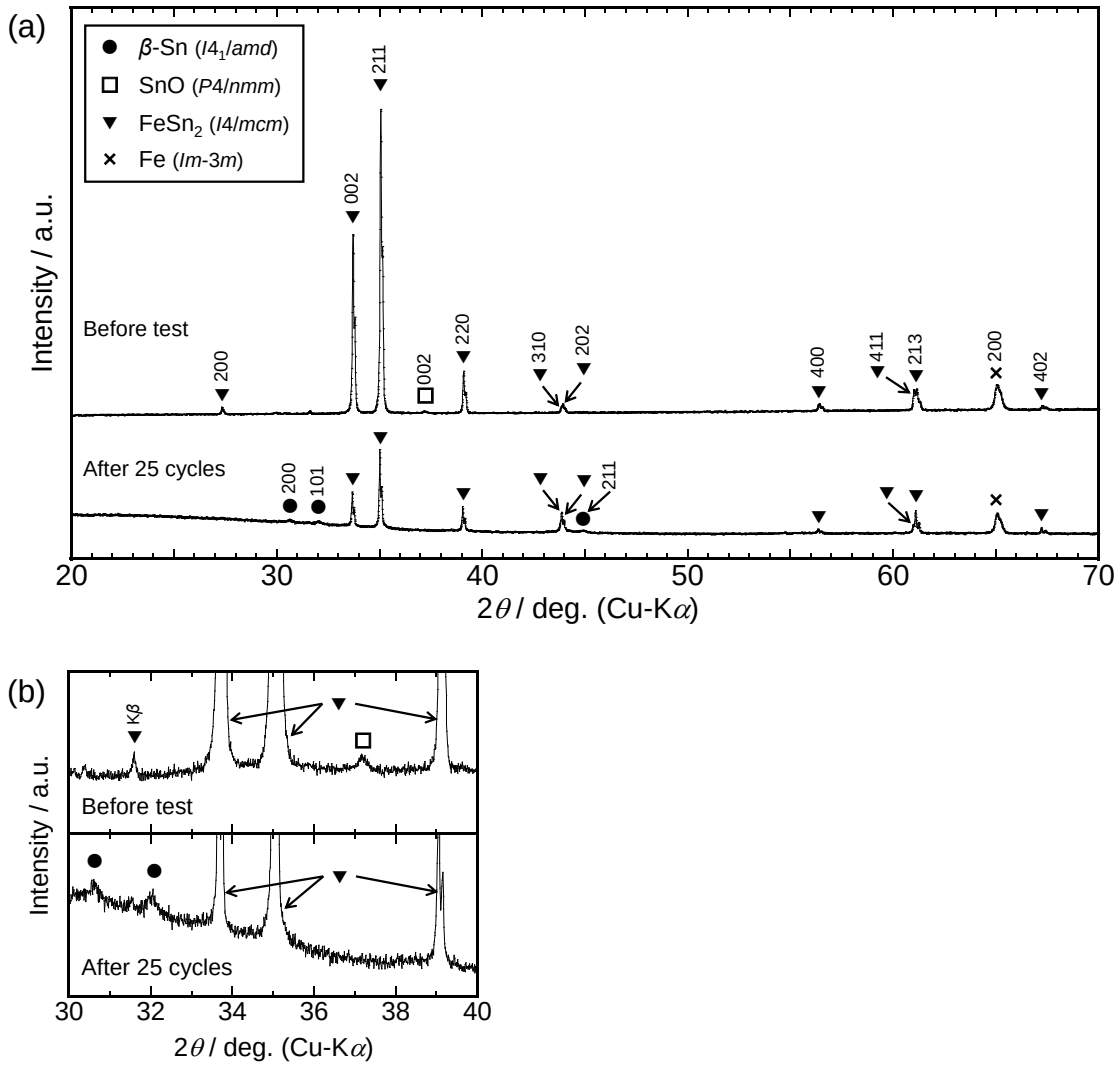

Fig. 9. (a) XRD patterns of $FeSn_2$ film before and after charge–discharge test. (b) Enlarged views of the XRD patterns of $FeSn_2$ film before and after 25 cycles of charge–discharge.

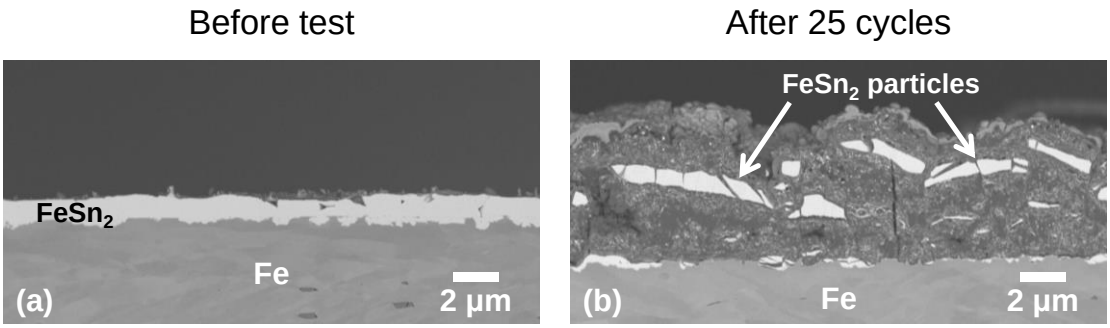

Fig. 10. Representative cross-sectional FE-SEM images of $FeSn_2$ film (a) before and (b) after 25 cycles of charge–discharge.

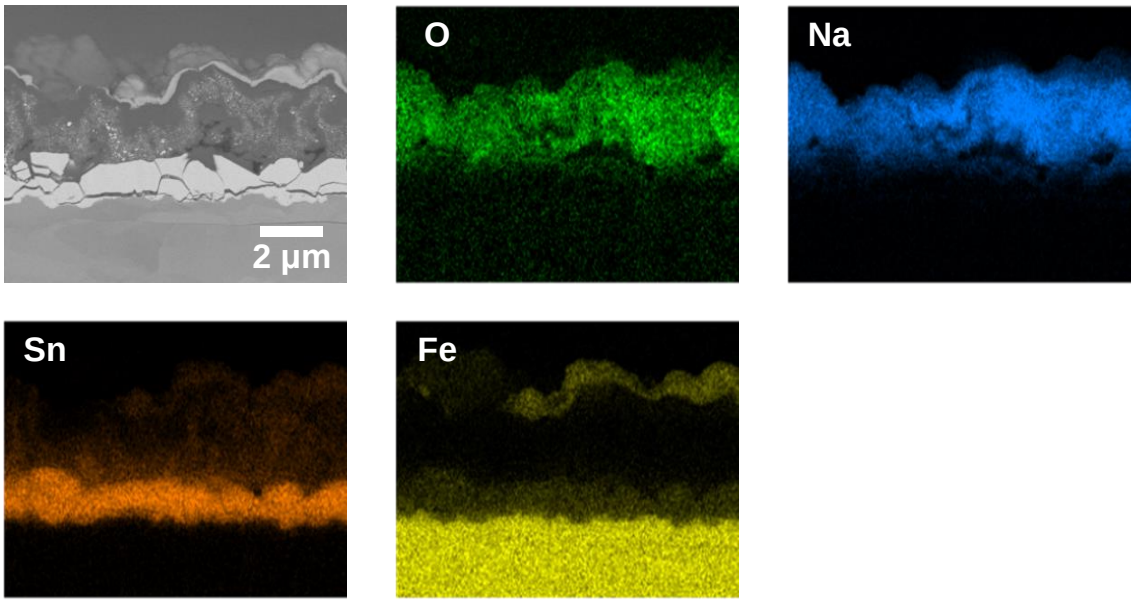

Fig. 11. A selected cross-sectional FE-SEM image and EDX mapping for the 25h-annealed film after 25 cycles of charge–discharge.